Theoretical and Experimental Studies of KLi_6TaO_6 as a Li-Ion Solid Electrolyte

Nobuaki Suzuki, Joohwi Lee, Yumi Masuoka, Shingo Ohta, Tetsuro Kobayashi, and Ryoji Asahi*[†]

Toyota Central R&D Laboratories, Inc., Nagakute, Aichi 480-1192, Japan

ABSTRACT: We study a hexagonal oxide KLi_6TaO_6 (KLTO), proposed as a Li-ion solid electrolyte by using a recently developed screening method. First-principles calculations predict that KLTO presents a good Li-ion conductivity (σ_{Li}) and a low activation energy (E_a). Li migration is enhanced by the presence of excess Li ions in the interstitial region via a kick-out mechanism. Our experimental results demonstrate that Sn-doped KLTO presents a conductivity of 1×10^{-5} S cm^{-1}, a σ_{Li} of 6×10^{-6} S cm^{-1}, and a relatively low E_a of 36 kJ mol^{-1}, which confirm the validity of the proposed screening method. Conversely, detailed analyses of the microstructure and X-ray diffraction patterns of KLTO samples indicate that a stable Li-excess condition is not achieved, therefore, leaving potential improvement of the performance of KLTO as a Li-ion solid electrolyte by optimizing extrinsic doping and fabrication process.

1. Introduction

Owing to their high energy density, Li-ion batteries have been widely used for applications ranging from smart phones to airplane components. Given the increasing demand for energy density and safety, all-solid-state Li secondary batteries have attracted increasing attention because they can significantly outperform conventional battery systems. One of the key materials in all-solid-state Li batteries is the solid electrolyte with a high Li-ion conductivity. Recently, the search for new solid electrolytes has become a research hotspot. In particular, since $Li_{10}GeP_2S_{12}$ (LGPS) whose Li-ion conductivity (σ_{Li}) higher than 10^{-2} S cm^{-1}at 300 K was discovered, the sulfides have attracted increasing interest.[1] The ionic conductivity (σ) of $Li_{9.54}Si_{1.74}P_{1.44}S_{11.7}Cl_{0.3}$, which is a LGPS-type superionic conductor, was reported to be 2–3 times higher than that of liquid electrolytes.[2] Sulfides are considered good candidates for all-solid-state Li batteries; however, other types of solid electrolytes, such as oxides, present higher chemical stability and mechanical strength than sulfides. Among oxides, $Li_7La_3Zr_2O_{12}$ (LLZO), which is a garnet-type oxide, presents a high σ_{Li} (>10^{-4} S cm^{-1}), high chemical stability against metallic Li, and wide electrochemical window.[3] The search for new solid electrolytes with suitable properties for high performance Li-ion batteries is ongoing.

Recently, we developed a new screening method for the identification of potentially good Li conductors.[4] This method relies on the so-called corrugation descriptor to efficiently estimate the Li migration energy of materials using first-principles calculations, and thus allowed us to quickly screen the Li-containing oxides included in the Inorganic Crystal Structure Database.[5] The list of oxides with a low corrugation energy is summarized in Sec. S1 in Supporting Information (SI). Consequently, we determined that three oxides with a hexagonal crystal structure, namely KLi_6TaO_6 (KLTO),[6] KLi_6BiO_6 (KLBO),[7] and KLi_6IrO_6 (KLIO),[8] were good Li conductors with low corrugation energies. Among them Sn-doped KLBO has been recently proposed as a potential good Li conductor using first-principles molecular dynamics (FPMD) calculations;[9, 10] however, the theoretical results have not yet been validated experimentally. In addition, KLIO was not promising for all-solid-state Li batteries because it is almost metallic.

In this study, we evaluate the potential of KLTO as a Li-ion conductor. First-principles and FPMD calculations are performed to analyze the conductivity and migration mechanism of Li ions. We synthesize doped KLTO samples using Ta, Sn, Ti, Zr, Hf, and Fe as dopants. The samples are characterized by powder X-ray diffraction (XRD) and scanning electron microscopy (SEM) analyses. We then determine their σ_{Li} and activation energy (E_a), which are discussed with the theoretical predictions.

2. Method

2.1. Theoretical calculations

Figure 1(a) and Figure 1(b) present the hexagonal crystal structure of KLTO in a conventional $K_3Li_{18}Ta_3O_{18}$ cell with a R-$3m$ space group. The valences of K, Ta, and Li were 1+, 5+, and 1+, respectively. Figure 1(c) illustrates the trigonal crystal structure of KLTO in a $2 \times 2 \times 2$ primitive cell with the formula $K_8Li_{48}Ta_8O_{48}$. Cell transformations were performed using the SPGLIB software,[11] which was implemented in the PHONOPY code.[12, 13] The Li interstitial (Li_i) sites were identified using an empty space finder module implemented in the MedeA program.[14] The $9d$ Li_i sites, for which the multiplicity of the Wyckoff position corresponded to that in the conventional cell, were determined to be stable.

(a) (c)
(b)

O K Ta Li
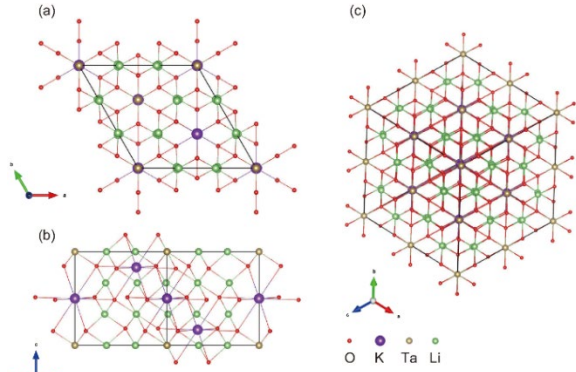
All first-principles calculations were performed using the projector augmented wave (PAW)[15, 16] method implemented in the Vienna *Ab-initio* Simulation Package.[17, 18] We used the exchange-correlation function of the generalized gradient approximation (GGA) parameterized in the Perdew–Burke–Ernzerhof (PBE) functional.[19] Structural optimizations of the primitive cells (14 atoms) with associated changes in lattice constants and atomic coordinates were performed until the interatomic force on each atom was reduced to within 0.005 eV Å^{-1}. The cutoff energy was set to 520 eV. The Brillouin zone was sampled using Γ-centered $4 \times 4 \times 4$ meshes with integration based on Gaussian smearing (width of 0.1 eV). Electronic spin polarizations were turned on, except for the case in which the up- and down-spins compensated each other. The bandgaps were calculated using a screened hybrid density functional parameterized by Heyd–Scuseria–Ernzerhof (HSE06)[20, 21] as well as the GGA.

The migration barrier energy (E_{mig}) was calculated using the climbing image nudged elastic band (CI-NEB) method[22, 23] with three intermediate images using a supercell (112 atoms) that was generated from a $2 \times 2 \times 2$ primitive cell. The CI-NEB method was employed using seven intermediate images. CI-NEB calculations were performed until the forces decreased below 0.03 eV Å^{-1} with a spring constant of 5 eV Å^{-2} between images. The k-space was sampled using Γ-centered $2 \times 2 \times 2$ meshes. We adopted a singly charged interstitial Li ion (Li$_i^+$) for E_{mig} calculations and assumed that this charged point defect was formed via extrinsic doping. Supercells with charged point defects were described by changing the number of electrons to compensate for the background charges.

To determine the Li-ion diffusivity (D_{Li}) of the samples, we performed FPMD calculations using a supercell of the same size as that used to calculate E_{mig}, which included one Li$_i$ atom randomly placed at a $9d$ site. We also adopted the Li point defect for FPMD calculations and assumed that the charged point defects were formed via extrinsic doping.

The D value of each element at high temperature was determined from the mean-square displacement (MSD) after a long simulation time (t) as follows:[24, 25]

$$D(t) = \lim_{t \to \infty} \frac{\text{MSD}}{6t}. \tag{1}$$

Here, MSD(t, t_0) can be calculated as:

$$\text{MSD}(t, t_0) = \frac{1}{n} \sum_i |r_i(t + t_0) - r_i(t_0)|^2, \tag{2}$$

where n is the number of atoms of each element, $r_i(t_0)$ and $r_i(t + t_0)$ are the positions of *the i-th atom* at the multiple time origin (t_0)

and new time ($t + t_0$), respectively. To improve the statistics, the MSD was smoothed by averaging the MSD (t, t_0) values. An interval of 1 fs was used for each atomic movement cycle. Temperature was increased from 573 K to the target temperature during the first 1000 cycles. Thereafter, FPMD was performed using the Nose thermostat[26, 27] with a canonical ensemble for 60 000 cycles and averaging the data over a period of 2–60 ps to calculate the MSD with sufficient movement of Li atoms after ignoring the first 2000 cycles. Three FPMD trials were performed at each temperature to calculate average D values. The isosurface of the Li-ion probability density distribution was obtained using the Pymatgen-diffusion module.[28] Atomic distribution data were collected every three ionic steps over a period of 2–60 ps.

We predicted the σ_{Li} values using the D_{Li} values at low temperature as follows. $D_{Li}(T)$ can be calculated using the Arrhenius equation

$$D_{Li}(T) = D_{Li,0} \exp\left(\frac{-E_a}{k_B T}\right)$$

or

$$\ln D_{Li}(T) = \ln D_{Li,0} - \frac{E_a}{k_B T}, \tag{3}$$

where $D_{Li,0}$ is the pre-exponential factor, k_B is the Boltzmann constant, and T is the absolute temperature. E_a was determined from the slope of the $\ln(D_{Li})$ vs. $1/T$ or $\ln(T \cdot \sigma_{Li})$ vs. $1000/T$ plots. $\sigma_{Li}(T)$ at the dilute level can be calculated using the $D_{Li}(T)$ values and the Nernst–Einstein equation as follows:[29, 30]

$$T \cdot \sigma_{Li}(T) = \frac{(ze)^2 n}{k_B} D_{Li}(T) = \frac{(ze)^2 n}{k_B} D_{Li,0} \exp\left(\frac{-E_a}{k_B T}\right) \tag{4}$$

where z is the valence of a Li ion, e (1.6×10^{-19} C) is the unit charge, and n is the ionic concentration of Li atoms in the computational cells of the oxides.

For computational efficiency, the cutoff energy was decreased to 300 eV, a soft pseudopotential with a low maximum cutoff energy (288 eV) was used for O, spin polarization was turned off, and only the Γ-point was used for k-space sampling. To accelerate the diffusion of Li atoms, we performed calculations in the high temperature range of 573–1273 K. The D_{Li} values of the analyzed quaternary oxides that did not undergo phase transitions were correctly determined, and the MSD values of the O atoms and cations other than Li calculated using FPMD were not greater than 1 Å^2 in the selected temperature range (data not reported).

2.2. Experimental procedure

As reported in Section 3.1, our theoretical results predicted that σ_{Li} of KLTO should increase when Li$_i^+$ ions are introduced. Therefore, aliovalent doped samples in which Sn replaced Ta were investigated. Appropriate amounts of precursor materials, namely KO$_2$, KTaO$_3$, Li$_2$O, and SnO$_2$ powder (>99.9% purity, Kojundo Chemical Laboratory Co. Ltd., Japan), were weighed to prepare K$_{1.1}$Li$_{6.3}$Ta$_{0.9}$Sn$_{0.1}$O$_6$ according to its nominal composition. Excess Li and K were used considering the previously reported loss of K and Li during synthesis.[6] The raw powder materials were mixed in an agate mortar and pestle in an Ar-filled dry box (dew point of approximately 250 K) and were subsequently added to an alumina crucible. Thereafter, the samples were calcined in an O$_2$ gas stream (1.5 L min^{-1}) at 1073 K for 5 h, and then in air at 1073 K for 7 h. The calcined samples were pulverized in an Ar-filled glove box (dew point of approximately 193 K) to avoid powder exposure to moisture in air.

No dense specimens were successfully prepared using the solid-state sintering process because significant K and/or Li loss occurred at a high sintering temperature required for sintering. Alternatively, we used the spark plasma sintering (SPS) method.[31] This method promotes quick sintering at a relatively low temperature. Calcined powder (5 g) mixed with additives was put into a graphite mold in an Ar-filled glove box, which was placed in the

SPS chamber. For an additive, Li_3BO_3 (5 wt.%) which is a known sintering additive effective for densification was used.[32] KO_2 was also used as an additive to compensate for the loss of K during SPS. To optimize the SPS conditions, we changed the sintering temperature from 973 to 1073 K and increased the amount of excess KO_2 added to the calcined powder up to 40 mol% (corresponding to $K_{1.5}Li_{6.3}Ta_{0.9}Ti_{0.1}O_6$). SPS was performed for 10 min at the specified temperature under a pressure of 50 MPa in an Ar atmosphere (−0.02 MPa).

We also examined the effects of Ti, Zr, Hf, and Fe as dopants using TiO_2, ZrO_2, HfO_2, and Fe_2O_3 (>99.9% purity, Kojundo Chemical Laboratory Co. Ltd., Japan) as precursors. The nominal compositions and SPS temperatures of all samples are summarized in Table 1.

Table 1. Synthesized samples: nominal compositions, amount of KO_2 additive, and spark plasma sintering (SPS) temperatures. The nominal compositions include the KO_2 additive listed in the second column. All samples underwent SPS for 10 min at the specified temperature under a 50 MPa pressure in an Ar atmosphere (−0.02 MPa).

Nominal composition	Amount of KO_2 added before SPS (mol%)	SPS temperature (K)
$K_{1.1}Li_{6.3}Ta_{0.9}Sn_{0.1}O_6$	0	973
$K_{1.1}Li_{6.3}Ta_{0.9}Sn_{0.1}O_6$	0	1023
$K_{1.3}Li_{6.3}Ta_{0.9}Sn_{0.1}O_6$	20	1023
$K_{1.4}Li_{6.3}Ta_{0.9}Sn_{0.1}O_6$	30	1023
$K_{1.5}Li_{6.3}Ta_{0.9}Sn_{0.1}O_6$	40	1023
$K_{1.4}Li_{6.3}Ta_{0.9}Sn_{0.1}O_6$	30	1073
$K_{1.5}Li_{6.3}Ta_{0.9}Sn_{0.1}O_6$	40	1073
$K_{1.5}Li_{6.3}Ta_{0.9}Ti_{0.1}O_6$	40	1073
$K_{1.5}Li_{6.3}Ta_{0.9}Zr_{0.1}O_6$	40	1073
$K_{1.5}Li_{6.3}Ta_{0.9}Hf_{0.1}O_6$	40	1073
$K_{1.5}Li_{6.3}Ta_{0.9}Fe_{0.1}O_6$	40	1073
$K_{1.5}Li_{6.3}TaO_6$ (non-doped)	40	1073

The density (ρ) of the samples was measured using the Archimedes' method. The relative density (ρ_R) was calculated as $\rho_R = \rho/\rho_0$, where ρ_0 is the ideal density calculated from the experimental lattice constant of KLTO.[6] The microstructure and elementary distribution of all samples were analyzed using field-emission scanning electron microscopy (FE-SEM) and energy dispersion X-ray spectroscopy (EDX). The electron accelerating voltage of the FE-SEM instrument was set to 10 kV. Crystal structures were identified using powder XRD data collected utilizing synchrotron radiation (15.5 keV) at the Aichi-SR center. The lattice parameters and site occupations were refined using the Rietveld analysis program, RIETAN-FP.[33] The diffraction data were calibrated by comparing the measured and calculated diffraction peak positions of NIST-CeO_2 standard powder.

The alternate current (AC) impedance of the samples was measured using an LCR meter (IM3536; Hioki Denki, Japan). Prior to measurements, the surface of the pellets was smoothed using sandpaper up to the 800 grade and polished utilizing a lapping film. Thereafter, Au electrodes were sputter-coated on both sides of the specimens. AC impedance measurements were performed in the frequency range of 4 Hz to 5 MHz at several tem-

peratures in the range of 300–473 K (an average of two measurements were taken with a 10 min interval after each temperature remained stable for 10 min) under a N_2 flow of 1.5 L min^{-1} to achieve a P_{O_2} of 10^{-5} atm.

The direct current (DC) σ and transference number of Li ions (t_{Li}) values were evaluated using a symmetric cell (Fig. 2). To block electronic contribution to conductivity, a 100 μm thick polymer electrolyte sheet was inserted between the Li metal electrode and the sample on each side of the cell.[34] The polymer electrolyte was prepared by adding lithium bis(trifluoromethylsulfonyl)imide (LiTFSI) to poly(ethylene oxide) (PEO) keeping a O:Li molar ratio of 10:1, where O is the ether oxygen in PEO. For the DC measurements, the changes in current with time at a constant bias voltage were measured for 10 h at 300 K. We also measured the AC impedances of the cell before and after DC measurements, and evaluated the interfacial resistances between the PEO-LiTFSI polymer electrolyte and sample. We also confirmed that the resistance between the polymer electrolyte and Li mental was negligible (less than 1/100 of the total resistance of the cell). The voltage drops within the sample during DC measurements were determined by compensating for the interfacial resistances and converted to DC conductivities of the sample using the currents measured initially and after 10 h. The t_{Li} value was then determined using the ratio of the DC σ value after 10 h to the initial DC σ value.

3. Results and discussion

3.1. Theoretical results and analysis

KLTO is a wide-bandgap insulator. Its bandgaps calculated using the GGA method in the PBE functional and HSE06 hybrid functional were 4.41 and 5.97 eV respectively. The calculated theoretical lattice parameters by the GGA method in the PBE functional ($a = 8.283$ Å, $b = 8.283$ Å, $c = 7.265$ Å, $\gamma = 120°$) were in agreement with previously reported experimental values ($a = 8.226$ Å, $b = 8.226$ Å, $c = 7.212$ Å, $\gamma = 120°$)[6] within the typical overestimation (less than 0.7%).

To calculate E_{mig} using the NEB method, Li_i atoms were considered to migrate between two 9d sites via a kick-out mechanism (Fig. 3(a)). A 9d site Li_i atom moved to 18f site kicking out the existing Li atom, and then the kicked-out Li atom moved to another Li_i 9d site. The migration path of Li_i was delocalized and connected to neighboring cells in three dimensions. The NEB results are presented in Fig. 3(c). The E_{mig} of Li_i was low (7.7 kJ mol^{-1}). Under stoichiometric conditions, a Frenkel pair of Li_i and $\square_{Li}$ (where $\square$ is a vacancy) was dynamically unstable (data not reported). Therefore, Li-excess conditions were critical for the formation of Li_i species with a low E_{mig}.
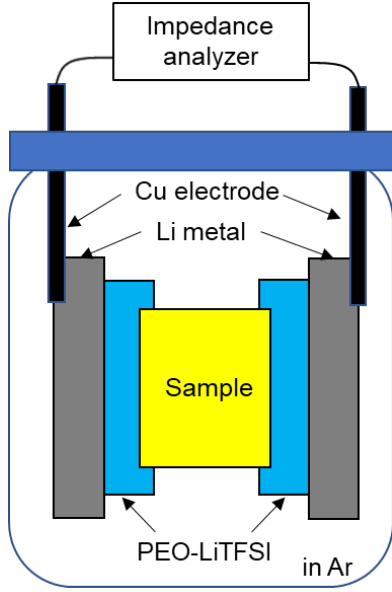
Figure 2. Schematic diagram of the symmetric cell used for direct current conductivity measurements. The cell was placed in an Ar-filled beaker and two Cu electrodes were connected to an impedance analyzer outside the beaker. Here, PEO-LiTFSI denotes poly(ethylene oxide)-bis(trifluoromethylsulphonyl)imide.
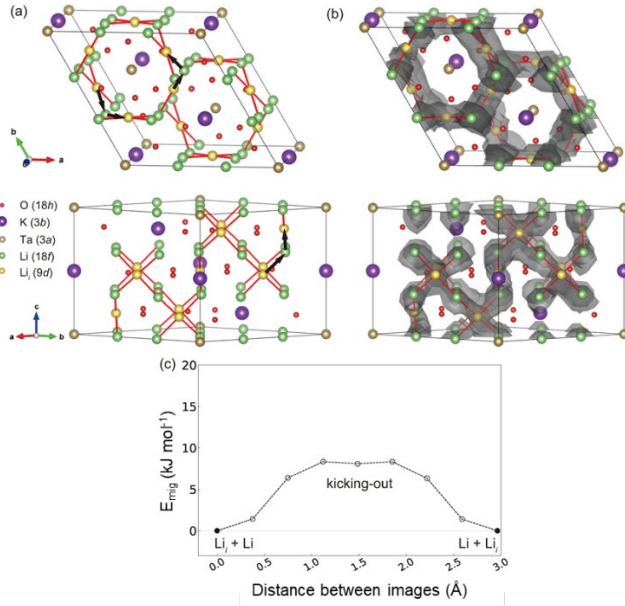

Figure 3. (a) Locations of a stable Li_i site ($9d$) and its migration path in KLi_6TaO_6 (KLTO). The identical migration paths are illustrated as connections between the Li_i ($9d$) and Li ($18f$) sites. The arrows illustrate Li migration via a kick-out mechanism. (b) Isosurface of Li_i ion probability density distribution (P; gray) in a conventional KLTO cell (0.3% of P_{max}) at 973 K obtained using first-principles molecular dynamics calculations. (c) Nudged elastic band profiles of a Li_i site of KLTO with a kick-out mechanism. The closed circles denote the initial and final states with a Li_i atom in the $9d$ site.

The dependence of the calculated (symbols) and fitted (lines) σ_{Li} values of KLTO on temperature determined using FPMD calculations is presented in Fig. 4. For KLTO under 5.6% and 2.1% Li excess conditions, the E_a values were 11 and 12 kJ mol^{-1}, respectively, which agreed well with the E_{mig} value determined

using the NEB method (7.7 kJ mol^{-1}). In addition, the trajectory of Li determined using FPMD calculations (Fig. 3(b)) was in agreement with the migration path with a low E_{mig} suggested using the NEB method (Fig. 3(a)). The σ_{Li} values of the KLTO samples with an additional Li_i atom prepared under 5.6% and 2.1% Li-excess conditions predicted using FPMD calculations at 300 K were 0.078 and 0.027 S cm^{-1}, respectively, which were comparable to those previously reported for Li-conducting sulfides ($\sigma_{Li} > 10^{-2}$ S cm^{-1}).[1, 2, 35] Conversely, under 2.1% Li-vacant conditions, σ_{Li} at 300 K was 6.9×10^{-5} S cm^{-1}, and E_a was 29 kJ mol^{-1}. In addition, under stoichiometric conditions, the D_{Li} value of the $K_8Li_{48}Ta_8O_{48}$ cell was 3.1×10^{-9} cm^2 s^{-1} at 1273 K, which was three orders of magnitude smaller than that of the KLTO with a Li_i atom prepared under 2.1% Li-excess conditions (4.4×10^{-6} cm^2 s^{-1}). This confirmed that in the absence of excess dopants or Li defects, KLTO was not expected to present Li conductivity.
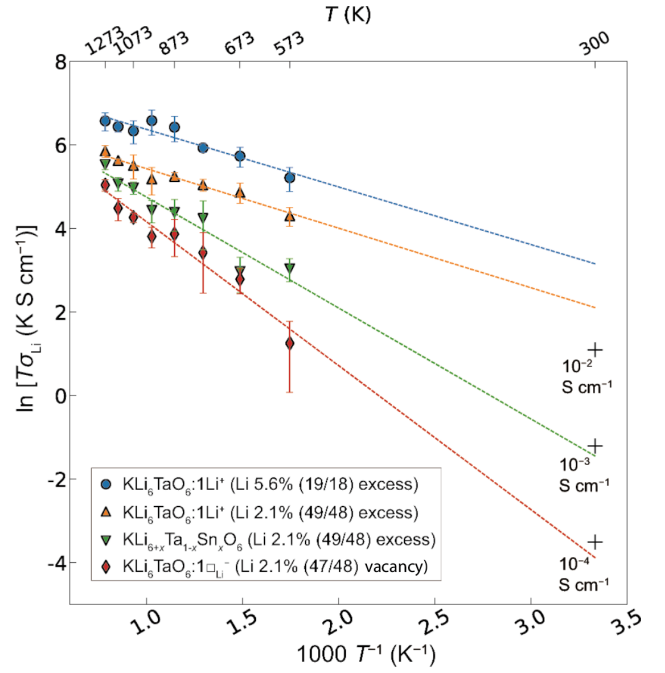

Figure 4. Dependence of calculated (symbols) and fitted (lines) Li-ionic conductivity (σ_{Li}) values of KLi_6TaO_6 (KLTO) on temperature (T). The error bars indicate one standard deviation. The "+" marks denote the σ_{Li} values at 300 K for reference.

Table 2. Measured and relative densities (ρ and ρ_R, respectively) and conductivities (σ) at 300 K of Sn-doped $K_xLi_{6.3}Ta_{0.9}Sn_{0.1}O_6$ (x = 1.1, 1.3, 1.4, 1.5) samples. The σ value of the $K_{1.3}Li_{6.3}Ta_{0.9}Sn_{0.1}O_6$ sample could not be determined using the Nyquist plot. Here, SPS denotes spark plasma sintering.

Sample	SPS conditions	ρ (g cm^{-3})	ρ_R (%)	σ (S cm^{-1})
$K_{1.1}Li_{6.3}Ta_{0.9}Sn_{0.1}O_6$	973 K, 10 min	3.77	89.4	2.0×10^{-6}
$K_{1.1}Li_{6.3}Ta_{0.9}Sn_{0.1}O_6$	1023 K, 10 min	3.82	90.7	3.3×10^{-6}
$K_{1.3}Li_{6.3}Ta_{0.9}Sn_{0.1}O_6$	1023 K, 10 min	3.33	79.0	−
$K_{1.4}Li_{6.3}Ta_{0.9}Sn_{0.1}O_6$	1023 K, 10 min	3.14	74.4	3.6×10^{-6}
$K_{1.5}Li_{6.3}Ta_{0.9}Sn_{0.1}O_6$	1023 K, 10 min	2.91	69.1	6.7×10^{-6}
$K_{1.4}Li_{6.3}Ta_{0.9}Sn_{0.1}O_6$	1073 K, 10 min	3.84	91.0	1.3×10^{-6}
$K_{1.5}Li_{6.3}Ta_{0.9}Sn_{0.1}O_6$	1073 K, 10 min	3.93	93.2	5.7×10^{-6}

The NEB and FPMD results provided a scientific rationale for the great potential of KLTO as a Li-ion conductor. Finding a reliable method to achieve Li-excess conditions is a challenge for practical applications. One such method, which has been successfully used for garnet-type oxides is aliovalent cation doping to compensate for charge imbalance.[36, 37] To analyze the effect of an extrinsic dopant on σ_{Li}, an acceptor cation Sn^{4+} was substituted with Ta^{5+} to compensate for the charge of the Li_i^+ ions. Then, σ_{Li} decreased to 7.8×10^{-4} S cm^{-1} at 300 K and E_a increased to 22 kJ mol^{-1}, compared to those without the extrinsic dopant (Fig. 4). These results were ascribed to the interactions between point defects. Furthermore, a detailed analysis of Sn-doped KLTO revealed that E_{mig} was 28 kJ mol^{-1} and a large energy barrier of 32 kJ mol^{-1} was present around the Sn_{Ta}^- sites, which quantitatively agreed with the high E_a of 22 kJ mol^{-1} in FPMD. This suggested that extrinsic dopant selection is important for achieving a high Li-ion conductivity.

3.2. Experimental results and discussion

The ρ_R and σ at 300 K (σ@300 K) values of the Sn-doped $K_xLi_{6.3}Ta_{0.9}Sn_{0.1}O_6$ (x = 1.1, 1.3, 1.4, 1.5) samples after SPS are listed in Table 2. The ρ_R values approached 90% in the $K_{1.1}Li_{6.3}Ta_{0.9}Sn_{0.1}O_6$ sample without excess KO_2, and decreased with increasing excess KO_2 amount at the same SPS temperature of 1023 K. Conversely, σ increased with increasing excess KO_2 amount. These results suggested that the excess KO_2 hindered sintering; however, it also compensated for the loss of K during sintering, contributing to the high σ values of the $K_xLi_{6.3}Ta_{0.9}Sn_{0.1}O_6$ samples. As the SPS temperature was increased from 1023 to 1073 K, ρ_R exceeded 90%; however, the σ value of the $K_{1.4}Li_{6.3}Ta_{0.9}Sn_{0.1}O_6$ sample was lower than those of all other $K_xLi_{6.3}Ta_{0.9}Sn_{0.1}O_6$ samples probably because of the loss of K with increasing SPS temperature. Lastly, the $K_{1.5}Li_{6.3}Ta_{0.9}Sn_{0.1}O_6$ sample that underwent SPS at 1073 K presented high ρ_R and σ values.

The SEM secondary electron images of $K_xLi_{6.3}Ta_{0.9}Sn_{0.1}O_6$ are presented in Fig. 5. The microstructure of the $K_{1.1}Li_{6.3}Ta_{0.9}Sn_{0.1}O_6$ sample without excess KO_2 after SPS at 973 K was dense (Fig. 5 (a)), which was consistent with the high ρ_R of this sample. The excess KO_2 and SPS at 1023 K resulted in pore and precipitate formation (Figs. 5 (b)–(d)). After SPS at 1073 K, the $K_{1.5}Li_{6.3}Ta_{0.9}Sn_{0.1}O_6$ sample presented a dense microstructure (Fig. 5 (f)). The grains in the microstructure of the $K_{1.5}Li_{6.3}Ta_{0.9}Sn_{0.1}O_6$ sample that underwent SPS at 1073 K (Fig. 5(f)) were larger than those of the $K_{1.1}Li_{6.3}Ta_{0.9}Sn_{0.1}O_6$ sample that underwent SPS at 973 K (Fig. 5(a)).
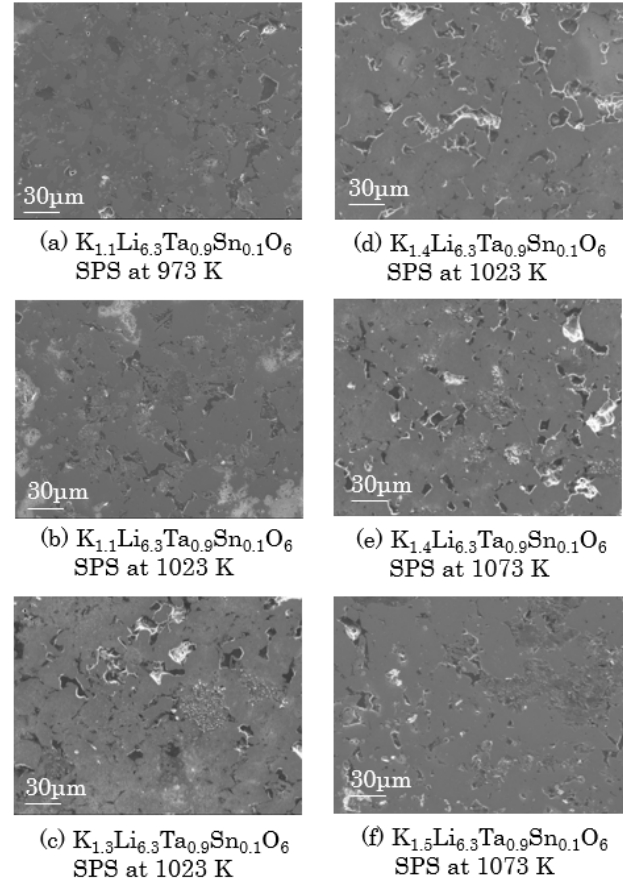

(a) $K_{1.1}Li_{6.3}Ta_{0.9}Sn_{0.1}O_6$ SPS at 973 K

(d) $K_{1.4}Li_{6.3}Ta_{0.9}Sn_{0.1}O_6$ SPS at 1023 K

(b) $K_{1.1}Li_{6.3}Ta_{0.9}Sn_{0.1}O_6$ SPS at 1023 K

(e) $K_{1.4}Li_{6.3}Ta_{0.9}Sn_{0.1}O_6$ SPS at 1073 K

(c) $K_{1.3}Li_{6.3}Ta_{0.9}Sn_{0.1}O_6$ SPS at 1023 K

(f) $K_{1.5}Li_{6.3}Ta_{0.9}Sn_{0.1}O_6$ SPS at 1073 K

Figure 5. Scanning electron microscopy secondary electron images of $K_xLi_{6.3}Ta_{0.9}Sn_{0.1}O_6$ (x = 1.1, 1.4, 1.5) samples sintered at various spark plasma sintering temperatures.

This was further observed in back scattered electron images and elementary EDX mappings of the $K_{1.1}Li_{6.3}Ta_{0.9}Sn_{0.1}O_6$ and $K_{1.5}Li_{6.3}Ta_{0.9}Sn_{0.1}O_6$ samples (Figs. 6 (a) and (b), respectively). EDX is not a quantitatively accurate method and presents a low energy sensitivity for Li; however, the overall phase distribution of the analyzed samples can be evaluated using their EDX mapping images. For the $K_{1.1}Li_{6.3}Ta_{0.9}Sn_{0.1}O_6$ sample that underwent SPS at 973 K, the KLTO phase (Area C, Fig. 6 (a)) consisted of small grains, which were isolated by a surrounding Ta-rich/K-poor secondary phase (Area E, Fig. 6 (a)) and voids, though the bulk phase was mostly in the single phase of KLTO (Fig. S3 in SI). Conversely, for the $K_{1.5}Li_{6.3}Ta_{0.9}Sn_{0.1}O_6$ sample that under-

went SPS at 1073 K, the KLTO phase (Area E in Fig. 6 (b)) consisted of large grains, which were interconnected throughout the solid, and only traces of a Ta-rich/K-poor secondary phase were observed (Areas A and B, Fig. 6 (b), and Fig. S3 in SI). These results suggested that the excess KO_2 can effectively decrease the amount of Ta-rich/K-poor secondary phase and promote the grain growth of the KLTO phase, probably because it compensated for the loss of K during SPS. Such larger grains can contribute to a high σ value, as indicated in Table 2, while the small isolated secondary phase could not affect σ so much. The KLTO phase did not contain a detectable amount of Sn (Area C, Fig. 6 (a) and Area E, Fig. 6 (b)); instead, Sn segregation was observed around the grain boundaries (Area D, Fig. 6 (a) and Area D, Fig. 6(b)).
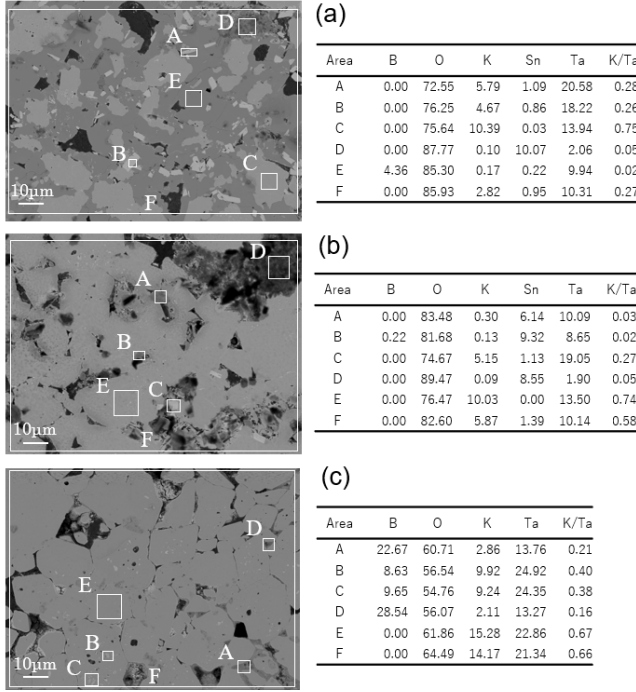

(a)

Area	B	O	K	Sn	Ta	K/Ta
A	0.00	72.55	5.79	1.09	20.58	0.28
B	0.00	76.25	4.67	0.86	18.22	0.26
C	0.00	75.64	10.39	0.03	13.94	0.75
D	0.00	87.77	0.10	10.07	2.06	0.05
E	4.36	85.30	0.17	0.22	9.94	0.02
F	0.00	85.93	2.82	0.95	10.31	0.27

(b)

Area	B	O	K	Sn	Ta	K/Ta
A	0.00	83.48	0.30	6.14	10.09	0.03
B	0.22	81.68	0.13	9.32	8.65	0.02
C	0.00	74.67	5.15	1.13	19.05	0.27
D	0.00	89.47	0.09	8.55	1.90	0.05
E	0.00	76.47	10.03	0.00	13.50	0.74
F	0.00	82.60	5.87	1.39	10.14	0.58

(c)

Area	B	O	K	Ta	K/Ta
A	22.67	60.71	2.86	13.76	0.21
B	8.63	56.54	9.92	24.92	0.40
C	9.65	54.76	9.24	24.35	0.38
D	28.54	56.07	2.11	13.27	0.16
E	0.00	61.86	15.28	22.86	0.67
F	0.00	64.49	14.17	21.34	0.66

Figure 6. Back scattered electron images of (a) $K_{1.1}Li_{6.3}Ta_{0.9}Sn_{0.1}O_6$ sample that underwent spark plasma sintering (SPS) at 973 K, (b) $K_{1.5}Li_{6.3}Ta_{0.9}Sn_{0.1}O_6$ sample that underwent SPS at 1073 K, and (c) $K_{1.5}Li_{6.3}TaO_6$ sample that underwent SPS at 1073 K. The numbers in the table represent the compositions in atom% and the K/Ta atomic ratios determined using energy-dispersive X-ray spectroscopy analysis for the areas marked in the images on the left.

The Rietveld analysis results for the powder XRD data of the $K_{1.5}Li_{6.3}Ta_{0.9}Sn_{0.1}O_6$ sample that underwent SPS at 1073 K are presented in Fig. 7. The major and minor peaks were attributed to the KLTO and Li_7TaO_6 phases, respectively. Rietveld analysis indicated that the Li_7TaO_6 phase content of this sample was 1.8%, and the Ta-rich/K-poor secondary phase observed in the EDX mappings was consistently identified as Li_7TaO_6. The excess KO_2 effectively compensated for the loss of K during SPS and reduced the content of Li_7TaO_6 phase in the $K_xLi_{6.3}Ta_{0.9}Sn_{0.1}O_6$ samples. Another important result derived from the Rietveld analysis was the site occupancy of Sn. We achieved the best convergence when Sn occupied just 2% of the Ta sites, which was lower than the nominal doping level of 10%. In addition, significant Li vacancy was indicated. These results suggested that Sn doping could not effectively introduce excess Li^+ ions. We will discuss the formation of Li_i^+ with conductivities and theoretical analysis later.
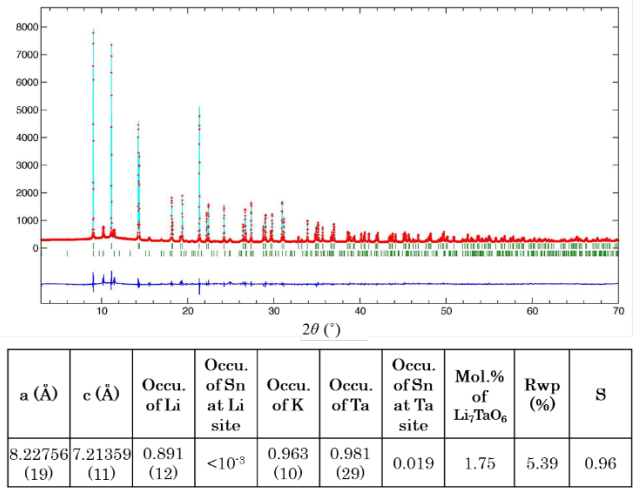

a (Å)	c (Å)	Occu. of Li	Occu. of Sn at Li site	Occu. of K	Occu. of Ta	Occu. of Sn at Ta site	Mol.% of Li_7TaO_6	Rwp (%)	S
8.22756 (19)	7.21359 (11)	0.891 (12)	$<10^{-3}$	0.963 (10)	0.981 (29)	0.019	1.75	5.39	0.96

Figure 7. Rietveld analysis of the $K_{1.5}Li_{6.3}Ta_{0.9}Sn_{0.1}O_6$ sample subjected to spark plasma sintering at 1073 K. The red dots, cyan lines, upper green vertical bars, lower green vertical bars, and blue lines represent the observed intensity, calculated intensity, peak position of KLi_6TaO_6, peak position of Li_7TaO_6, and errors, respectively. The table summarizes the lattice parameters (a and c), site occupancies (occ.), and Rietveld analysis convergent parameters (R_{wp} and S) considering that the secondary phase consisted of Li_7TaO_6. For this analysis, we assumed that no vacancies were available for the Ta sites where either Ta or Sn thus occupies.

Next, we examined Ti, Zr, Hf, and Fe dopants, in search of a better dopant than Sn. Based on the aforementioned data for Sn-doped KLTO, we focused on $K_{1.5}Li_{6.3}Ta_{0.9}M_{0.1}O_6$ (M = Ta, Sn, Ti, Zr, Hf, and Fe) samples that underwent SPS at 1073 K. The nominal compositions and ρ and ρ_R values of the samples after SPS are listed in Table 3. A non-doped sample was also synthesized and was used as the reference. The ρ_R values of all samples were higher than 90%.

Table 3. Measured and relative densities (ρ and ρ_R, respectively) of non-doped and doped $K_{1.5}Li_{6.3}Ta_{0.9}M_{0.1}O_6$ (M = Ta, Ti, Zr, Hf, Sn and Fe) samples that underwent spark plasma sintering at 1073 K for 10 min.

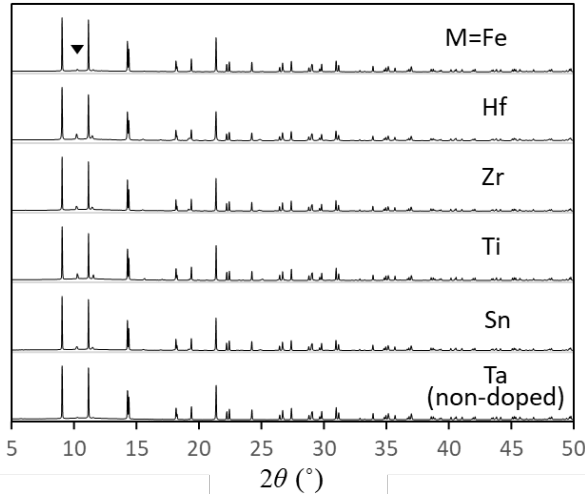| Sample	ρ (g cm^{-3})	ρ_R (%)
$K_{1.5}Li_{6.3}TaO_6$ (non-doped)	3.93	93.3
$K_{1.5}Li_{6.3}Ta_{0.9}Ti_{0.1}O_6$	4.05	96.0
$K_{1.5}Li_{6.3}Ta_{0.9}Zr_{0.1}O_6$	3.96	94.0
$K_{1.5}Li_{6.3}Ta_{0.9}Hf_{0.1}O_6$	3.93	93.2
$K_{1.5}Li_{6.3}Ta_{0.9}Sn_{0.1}O_6$	3.93	93.2
$K_{1.5}Li_{6.3}Ta_{0.9}Fe_{0.1}O_6$	3.85	91.4

Figure 8. Powder X-ray diffraction patterns of $K_{1.5}Li_{6.3}Ta_{0.9}M_{0.1}O_6$ (M = Ta, Sn, Ti, Zr, Hf, and Fe) samples after spark plasma sintering. All samples consisted mostly of single phase KLi_6TaO_6, and traces of Li_7TaO_6 were present as the secondary phase (▼).

The powder XRD patterns of the $K_{1.5}Li_{6.3}Ta_{0.9}M_{0.1}O_6$ (M = Ta, Sn, Ti, Zr, Hf, and Fe) samples after SPS are illustrated in Fig. 8. The peaks of the KLTO phase were dominant in the patterns of all samples, whereas a trace Li_7TaO_6 phase was observed, particularly in the XRD patterns of the Ti-, Zr-, and Hf-doped samples. The lattice parameters of the samples were determined via Rietveld analysis (Sec. S3 in SI). The lattice parameter a of the $K_{1.5}Li_{6.3}Ta_{0.9}M_{0.1}O_6$ (M = Ta, Sn, Ti, Zr, Hf, and Fe) samples and ionic radii of the doped ions, (Sn^{4+}, Ti^{4+}, Zr^{4+}, Hf^{4+}, and Fe^{3+}) in octahedral coordination are presented in Fig. 9. The changes in the lattice parameter a were mostly proportional to the ionic radii of the doped ions. Similar changes were obtained for the lattice parameter c. These results may suggest that the samples consist of solid solution of dopants, according to the Vegard's law. A detailed comparison of site occupancy for the $K_{1.5}Li_{6.3}Ta_{0.9}M_{0.1}O_6$ (M = Ta, Sn, Ti, Zr, Hf, and Fe) samples is not presented because we could not systematically reach Rietveld analysis convergence for the doped samples. However, the doped samples can present similar doping levels to the Sn-doped sample, a few % for the Ta sites, as inferred from the results in Figs. 7 and 9.
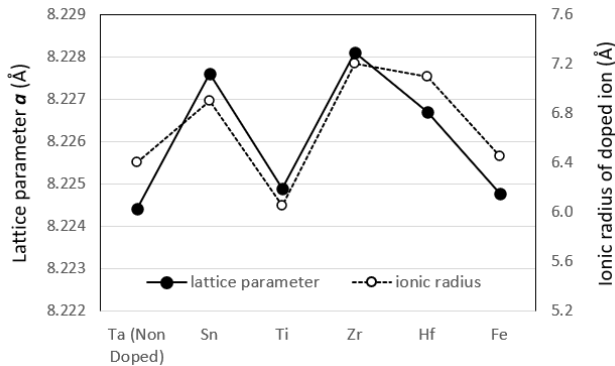

Figure 9. Lattice parameter a of $K_{1.5}Li_{6.3}Ta_{0.9}M_{0.1}O_6$ (M = Ta, Sn, Ti, Zr, Hf, and Fe) samples that underwent spark plasma sintering determined using Rietveld analysis and ionic radii of doped ions.

The bulk σ values of the synthesized samples determined via impedance measurements are illustrated in Fig. 10. The linear dependence of ln($T\sigma$) of 1000/T allowed us to determine the E_a

values of the samples by fitting the data. The σ and E_a values of the $K_{1.5}Li_{6.3}Ta_{0.9}M_{0.1}O_6$ (M = Ta (non-doped), Ti, Zr, Hf, Sn, and Fe) samples are summarized in Table 4. The Sn-doped sample presented the highest σ@300 K of 1×10^{-5} S cm^{-1} and the lowest E_a of 35.9 kJ mol^{-1} of all samples. The σ@300 K and E_a values of the Zr- and Hf-doped samples were slightly lower and higher, respectively, than those of the Sn-doped sample, and the σ@300 K and E_a values of the Ti- and Fe-doped samples were not significantly different from those of the non-doped sample. The σ@473 K values of all samples were similar. This suggested that a pre-exponential factor of $T\sigma$, which was sensitive to the number of active Li ions responsible for conductivity (Eq. 4), was not significantly affected by the dopants we studied.
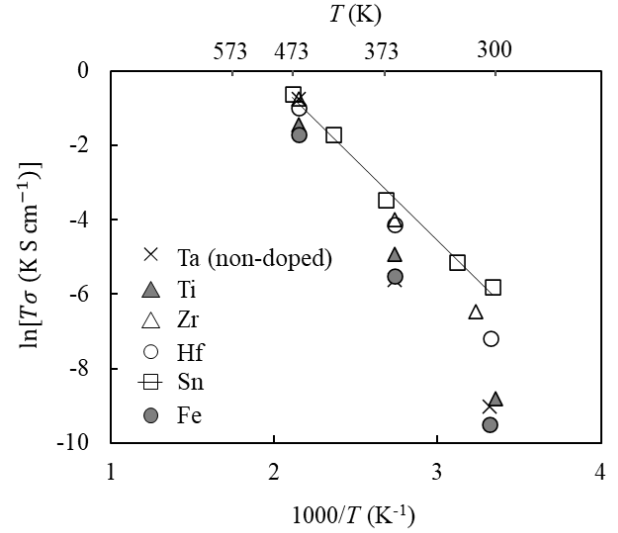

Figure 10. Logarithmic plot of conductivity (σ) of $K_{1.5}Li_{6.3}Ta_{0.9}M_{0.1}O_6$ (M = Ta, Ti, Zr, Hf, Sn, and Fe) vs. 1000/T. The data for the Sn-doped sample (solid line) were fitted and the activation energy of the sample was determined to be 35.9 kJ mol^{-1}.

Table 4. Conductivities (σ) at 300 and 473 K and activation energies (E_a) of the $K_{1.5}Li_{6.3}Ta_{0.9}M_{0.1}O_6$ (M = Ti, Zr, Hf, Sn, and Fe) samples that underwent spark plasma sintering at 1073 K for 10 min.

Sample	σ@300 K (S cm^{-1}) σ@473 K (S cm^{-1})	E_a (kJ mol^{-1})
$K_{1.5}Li_{6.3}TaO_6$ (non-doped)	4.0×10^{-7} 1.0×10^{-3}	55.1
$K_{1.5}Li_{6.3}Ta_{0.9}Ti_{0.1}O_6$	5.0×10^{-7} 5.0×10^{-4}	50.7
$K_{1.5}Li_{6.3}Ta_{0.9}Zr_{0.1}O_6$	5.0×10^{-6} 1.0×10^{-3}	43.8
$K_{1.5}Li_{6.3}Ta_{0.9}Hf_{0.1}O_6$	2.5×10^{-6} 8.0×10^{-4}	43.9
$K_{1.5}Li_{6.3}Ta_{0.9}Sn_{0.1}O_6$	1.0×10^{-5} 1.1×10^{-3}	35.9
$K_{1.5}Li_{6.3}Ta_{0.9}Fe_{0.1}O_6$	2.5×10^{-7} 3.9×10^{-4}	55.3

Table 5. Direct current conductivities (σ) and transference numbers of Li ions (t_{Li}) of the $K_{1.5}Li_{6.3}Ta_{0.9}Sn_{0.1}O_6$ sample evaluated using the symmetric cell illustrated in Fig. 2. The t_{Li} values were calculated as the ratio of σ after 10 h to the initial σ. The constant bias voltage was varied in the range of 0.5 to 1.5 V. The t_{Li} values were averaged to calculate t_{Li} ave.

	σ (S cm^{-1})				t_{Li} ave.
Voltage (V)	0.5	0.8	1.0	1.5	
Initial	1.15×10^{-5}	1.06×10^{-5}	1.08×10^{-5}	1.04×10^{-5}	
after 10 h	6.09×10^{-6}	6.66×10^{-6}	6.50×10^{-6}	5.16×10^{-6}	
t_{Li}	0.53	0.63	0.60	0.50	0.57

The t_{Li} value at 300 K measured from the DC σ values of the $K_{1.5}Li_{6.3}Ta_{0.9}Sn_{0.1}O_6$ sample using the symmetric cell illustrated in Fig. 2 are summarized in Table 5. The initial DC σ value was in good agreement with the σ value determined using AC impedance measurements (Table 4). The DC σ values were reproducible with respect to the different constant bias voltages, and the average t_{Li} was calculated to be 57%. The net σ_{Li} at 300 K of the $K_{1.5}Li_{6.3}Ta_{0.9}Sn_{0.1}O_6$ sample was determined to be 6×10^{-6} S cm^{-1}. We did not identify the other species in the residual transference numbers; however, we hypothesized that one of the residual species was K, as evidenced with its inhomogeneous distribution illustrated in Fig. 6.

The experimental σ_{Li} at 300 K and E_a values of the $K_{1.5}Li_{6.3}Ta_{0.9}Sn_{0.1}O_6$ sample (6×10^{-6} S cm^{-1} and 36 kJ mol^{-1}, respectively) were compared with the theoretical ones. The Sn-doped theoretical model (Fig. 4) was built using a 2.1% Li-excess where one of eight Ta atoms was substituted by Sn; therefore, the Sn concentration of the theoretical model was similar to the nominal composition of the experimental sample, and the σ_{Li} at 300 K and E_a values of the theoretical model were 7.8×10^{-4} S cm^{-1} and 22 kJ mol^{-1}, respectively. Conversely, the predicted σ_{Li} at 300 K and E_a values of the 2.1% Li-vacant model were 6.9×10^{-5} S cm^{-1} and 29 kJ mol^{-1}, respectively, which were in better agreement with the experimental results. According to the theoretical analysis, the Li_i^+ ions contribute to the high σ_{Li} values of the samples. On the other hand, defect formation energies obtained by the first-principles calculations showed the formation of $\square_{Li}^-$ was more stable than that of Li_i^+ or $(Sn_{Ta}^- + Li_i^+)^0$ (Sec. S2 in SI). This suggests that the existence of $\square_{Li}^-$ obstructs the formations of the active Li_i^+ ions in the crystal. In fact, $\square_{Li}^-$ was suggested by the Rietveld analysis (Fig. 7) and almost no dopant (within a variation in the EDX analysis) was observed in the matrix phase of the observed microstructure (Figs. 6 (a) and (b)). Instead, when comparing the microstructure of the Sn-doped and non-doped samples (Figs. 6 (b) and (c), respectively), we concluded that Sn doping promoted grain growth and, thus, lowered the rate-limiting diffusion barrier at grain boundaries. This was consistent with the observation that the pre-exponential factors of σ of all samples were similar (Fig. 10).

4. Conclusions

In this study, we provided theoretical and experimental data supporting the potential of KLTO as a good Li-ion conductor. Our theoretical study based on first-principles calculations predicted good σ_{Li} and low E_a values with a kick-out Li migration mechanism once excess Li_i^+ species were introduced. The experimentally determined σ, σ_{Li}, and E_a values of the Sn-doped sample were 1×10^{-5} S cm^{-1}, 6×10^{-6} S cm^{-1}, and 36 kJ mol^{-1}, respectively. The σ_{Li} value of the Sn-doped sample was comparable to those of previously reported LiPON[38] and $Li_2Ti_3O_7$ (c-axis)[39] Li-ion conductors. Moreover, the E_a value of the Sn-doped sample was as low as those of LLZO and $(LiLa)TiO_3$.[40] Therefore, in this study we demonstrated the effectiveness of our screening method based on the corrugation descriptor, which proposes solids with low E_a

values. Conversely, it was suggested that the dopants used in this study were not effectively present in the KLTO matrix and did not introduce stable Li^+ ions in the KLTO matrix, which could limit the experimental σ_{Li} values. This leaves the challenge of achieving stable Li-excess conditions by selecting adequate extrinsic dopants and processing conditions.

ASSOCIATED CONTENT

Supporting Information

The Supporting Information is available free of charge via the Internet at

https://xxxxx

Screening list identified by corrugation descriptor, defect formation energy, supplemental results of the Rietveld analysis, and microstructures of the Sn-doped samples (PDF).

AUTHOR INFORMATION

Corresponding Author

*E-mail: ryoji.asahi@chem.material.nagoya-u.ac.jp

Present Addresses

†Present affiliation: Nagoya University, Nagoya, Aichi 464-8603, Japan

Author Contributions

J.L. and R.A. screened database and J.L. performed theoretical calculations. N.S., Y.M., and R.A. conducted sample syntheses and evaluations, and S.O., T.K., and R.A. measured DC conductivities and transference numbers. R.A. designed the work. All authors contributed to drafting the manuscript and have given approval to the final version of the manuscript.

ABBREVIATIONS

AC, alternate current; CI-NEB, climbing image nudged elastic band; DC direct current; EDX, energy dispersion X-ray spectroscopy; FE-SEM field-emission scanning electron microscopy; FPMD, first-principles molecular dynamics; GGA, generalized gradient approximation; HSE, Heyd–Scuseria–Ernzerhof; KLIO, KLi_6IrO_6; KLTO, KLi_6TaO_6; LGPS, $Li_{10}GeP_2S_{12}$; LiTFSI, lithium

bis(trifluoromethylsulfonyl)imide; LLZO, $Li_7La_3Zr_2O_{12}$; MSD, mean-square displacement; PEO, poly(ethylene oxide); PBE, Perdew–Burke–Ernzerhof; SEM, scanning electron microscopy; SPS, spark plasma sintering; XRD, X-ray diffraction.

REFERENCES

1. Kamaya, N.; Homma, K.; Yamakawa, Y.; Hirayama, M.; Kanno, R.; Yonemura, M.; Kamiyama, T.; Kato, Y.; Hama, S.; Kawamoto, K.; Mitsui, A., A lithium superionic conductor. *Nat. Mater.* **2011,** *10*, 682‑686.

2. Kato, Y.; Hori, S.; Saito, T.; Suzuki, K.; Hirayama, M.; Mitsui, A.; Yonemura, M.; Iba, H.; Kanno, R., High-power all-solid-state batteries using sulfide superionic conductors. *Nat. Energy* **2016,** *1*, 16030.

3. Buschmann, H.; Dolle, J.; Berendts, S.; Kuhn, A.; Bottke, P.; Wilkening, M.; Heitjans, P.; Senyshyn, A.; Ehrenberg, H.; Lotnyk, A.; Duppel, V.; Kienle, L.; Janek, J., Structure and dynamics of the fast lithium ion conductor "$Li_7La_3Zr_2O_{12}$". *Phys. Chem. Chem. Phys.* **2011,** *13*, 19378‑19392.

4. France-Lanord, A.; Asahi, R.; Leblanc, B.; Lee, J.; Wimmer, E., Highly efficient evaluation of diffusion networks in Li ionic conductors using a 3D-corrugation descriptor. *Scientific reports* **2019,** *9*, 15123.

5. Belsky, A.; Hellenbrandt, M.; Karen, V. L.; Luksch, P., New developments in the Inorganic Crystal Structure Database (ICSD): Accessibility in support of materials research and design. *Acta Crystallogr., Sect. B: Struct. Crystallogr. Cryst. Chem.* **2002,** *58*, 364‑369.

6. Scheld, W.; Wehrum, G.; Hoppe, R., Ein neues Oxotantalat (V): Über $KLi_6[TaO_6]$ [1]. *Z. Anorg. Allg. Chem.* **1993,** *619*, 337‑342.

7. Huebenthal, R.; Hoppe, R., The First Guaternary Oxobismuthate (V): KLi_6BiO_6. *Acta Chem. Scand.* **1991,** *45*, 805‑811.

8. Kroeschell, P.; Hoppe, R., Ein neues Oxoiridat (V): $KLi_6[IrO_6]$. *Z. Anorg. Allg. Chem.* **1986,** *537*, 106‑114.

9. He, X.; Bai, Q.; Liu, Y.; Nolan, A. M.; Ling, C.; Mo, Y., Crystal Structural Framework of Lithium Super‑Ionic Conductors. *Adv. Energy Mater.* **2019,** *9*, 1902078.

10. Zhang, Y.; He, X.; Chen, Z.; Bai, Q.; Nolan, A. M.; Roberts, C. A.; Banerjee, D.; Matsunaga, T.; Mo, Y.; Ling, C., Unsupervised discovery of solid-state lithium ion conductors. *Nat. Commun.* **2019,** *10*, 5260.

11. Togo, A.; Tanaka, I., Spglib : a software library for crystal symmetry search. *arXiv:1808.01590* **2018**, 1‑11.

12. Togo, A.; Oba, F.; Tanaka, I., First-principles calculations of the ferroelastic transition between rutile-type and $CaCl_2$-type SiO_2 at high pressures. *Phys. Rev. B* **2008,** *78*, 134106.

13. Togo, A.; Chaput, L.; Tanaka, I.; Hug, G., First-principles phonon calculations of thermal expansion in Ti_3SiC_2, Ti_3AlC_2, and Ti_3GeC_2. *Phys. Rev. B* **2010,** *81*, 174301.

14. MedeA version 3.0. Materials Design, Inc., San Diego, U.S.A.

15. Blöchl, P. E., Projector augmented-wave method. *Phys. Rev. B* **1994,** *50*, 17953‑17979.

16. Kresse, G.; Joubert, D., From ultrasoft pseudopotentials to the projector augmented-wave method. *Phys. Rev. B* **1999,** *59*, 1758‑1775.

17. Kresse, G.; Furthmüller, J., Efficiency of Ab-Initio Total Energy Calculations for Metals and Semiconductors Using a Plane-Wave Basis Set. *Comput. Mater. Sci.* **1996,** *6*, 15‑50.

18. Kresse, G.; Furthmüller, J., Efficient Iterative Schemes for Ab Initio Total-Energy Calculations Using a Plane-Wave Basis Set. *Phy. Rev. B* **1996,** *54*, 11169‑11186.

19. Perdew, J. P.; Burke, K.; Ernzerhof, M., Generalized Gradient Approximation Made Simple. *Phys. Rev. Lett.* **1996,** *77*, 3865‑3868.

20. Heyd, J.; Scuseria, G. E.; Ernzerhof, M., Erratum: "Hybrid functionals based on a screened Coulomb potential" [J. Chem. Phys.118, 8207 (2003)]. *J. Chem. Phys.* **2006,** *124*, 219906.

21. Krukau, A. V.; Vydrov, O. A.; Izmaylov, A. F.; Scuseria, G. E., Influence of the exchange screening parameter on the performance of screened hybrid functionals. *J. Chem. Phys.* **2006,** *125*.

22. Henkelman, G.; Uberuaga, B. P.; Jónsson, H., A climbing image nudged elastic band method for finding saddle points and minimum energy paths. *J. Chem. Phys.* **2000,** *113*, 9901‑9904.

23. Henkelman, G.; Jónsson, H., Improved tangent estimate in the nudged elastic band method for finding minimum energy paths and saddle points. *J. Chem. Phys.* **2000,** *113*, 9978‑9985.

24. Oka, M.; Kamisaka, H.; Fukumura, T.; Hasegawa, T., DFT-based *ab initio* MD simulation of the ionic conduction in doped ZrO_2 systems under epitaxial strain. *Phys. Chem. Chem. Phys.* **2015,** *17*, 29057‑29063.

25. Bai, X.-M.; Zhang, Y.; Tonks, M. R., Strain effects on oxygen transport in tetragonal zirconium dioxide. *Phys. Chem. Chem. Phys.* **2013,** *15*, 19438‑19449.

26. Nosé, S., A unified formulation of the constant temperature molecular dynamics methods. *J. Chem. Phys.* **1984,** *81*, 511‑519.

27. Nosé, S., Constant temperature molecular dynamics methods. *Prog. Theor. Phys. Suppl.* **1991,** *103*, 1‑46.

28. Deng, Z.; Zhu, Z. Y.; Chu, I. H.; Ong, S. P., Data-Driven First-Principles Methods for the Study and Design of Alkali Superionic Conductors. *Chem. Mater.* **2017,** *29*, 281‑288.

29. Seko, A.; Koyama, Y.; Matsumoto, A.; Tanaka, I., First-principles molecular dynamics study for average structure and oxygen diffusivity at high temperature in cubic Bi_2O_3. *J. Phys.: Condens. Matter* **2012,** *24*, 475402.

30. Lee, J.; Ohba, N.; Asahi, R., First-principles prediction of high oxygen-ion conductivity in trilanthanide gallates Ln_3GaO_6. *Sci. Technol. Adv. Mater.* **2019,** *20*, 144‑159.

31. Munir, Z. A.; Anselmi-Tamburini, U.; Ohyanagi, M., The effect of electric field and pressure on the synthesis and consolidation of materials: A review of the spark plasma sintering method. *J. Mater. Sci.* **2006,** *41*, 763‑777.

32. Janani, N.; Deviannapoorani, C.; Dhivya, L.; Murugan, R., Influence of sintering additives on densification and Li+ conductivity of Al doped $Li_7La_3Zr_2O_{12}$ lithium garnet. *RSC Adv.* **2014,** *4*, 51228‑51238.

33. Izumi, F.; Momma, K., Three-Dimensional Visualization in Powder Diffraction. *Solid State Phenom.* **2007,** *130*, 15‑20.

34. Evans, J.; Vincent, C. A.; Bruce, P. G., Electrochemical measurement of transference numbers in polymer electrolytes. *Polymer* **1987,** *28*, 2324‑2328.

35. Mo, Y.; Ong, S. P.; Ceder, G., First principles study of the $Li_{10}GeP_2S_{12}$ lithium super ionic conductor material. *Chem. Mater.* **2011,** *24*, 15‑17.

36. Ohta, S.; Kobayashi, T.; Seki, J.; Asaoka, T., Electrochemical performance of an all-solid-state lithium ion battery with garnet-type oxide electrolyte. *J. Power Sources* **2012,** *202*, 332‑335.

37. Ohta, S.; Kobayashi, T.; Asaoka, T., High lithium ionic conductivity in the garnet-type oxide $Li_{7–x}La_3(Zr_{2–X}, Nb_X)O_{12}$ (X = 0‑2). *J. Power Sources* **2011,** *196*, 3342‑3345.

38. Yu, X. H.; Bates, J. B.; Jellison, G. E.; Hart, F. X., A stable thin-film lithium electrolyte: Lithium phosphorus

oxynitride. *J. Electrochem. Soc.* **1997,** *144*, 524‑532.

39.　　　Boyce, J. B.; Mikkelsen, J. C., Anisotropic conductivity in a channel-structured superionic conductor: $Li_2Ti_3O_7$. *Solid State Commun.* **1979,** *31*, 741‑745.

40.　　　Reddy, M. V.;　Julien, C. M.;　Mauger, A.; Zaghib, K., Sulfide and Oxide Inorganic Solid Electrolytes for All-Solid-State Li Batteries: A Review. *Nanomater.* **2020,** *10*.

SYNOPSIS TOC.

We study a hexagonal oxide KLi_6TaO_6 (KLTO), proposed as a Li-ion solid electrolyte by using a recently developed screening method. First-principles calculations predict that KLTO presents a good Li-ion conductivity (σ_{Li}) and a low activation energy (E_a) under the presence of excess Li ions. Our experimental results demonstrate that Sn-doped KLTO presents a conductivity of 1×10^{-5} S cm^{-1} and a low E_a of 36 kJ mol^{-1}, which confirm the validity of the proposed screening method. Detailed analyses indicate that a stable Li-excess condition is not achieved, therefore, leaving potential improvement of the performance of KLTO by optimizing extrinsic doping and fabrication process.